JSR Publications

Available Online

J. Sci. Res. **18** (1), 211-230 (2026)

JOURNAL OF SCIENTIFIC RESEARCH

www.banglajol.info/index.php/JSR

A Comprehensive Study of the Physical Properties of Actinide-based Advanced Nuclear Fuel Materials, UX (X = C, N, O): A DFT Insight

R. C. Karmkar*, E. Ahmed, B. K. Sarker, S. Ahmed, F. Hossain, M. T. Hossain, M. A. R. Sheikh

Bangladesh Atomic Energy Regulatory Authority (BAERA), E-12/A, Agargaon, Dhaka 1207, Bangladesh

Received 13 July 2025, accepted in final revised form 13 October 2025

Abstract

This investigation analyzes the fundamental physical properties of UX (X = C, N, O) using the density functional theory-based CGA-PBE and CGA-PBEsol functionals implemented in the CASTEP code. The obtained lattice parameters of UX using the CGA-PBEsol technique demonstrate good agreement with previously reported results, and further calculations have been performed based on this technique. The electronic structure analysis reveals the metallic nature of UX. The dynamical stability of the studied structures has been checked through their phonon dispersion curves. The mechanical stability and ductile behavior of the studied compounds have been confirmed by the Born stability criterion, Cauchy pressures, Pugh's ratio, and Poisson ratio. For the first time, the famous Slack equation has been utilized to calculate the lattice thermal conductivity of the studied compounds. From the thermophysical analysis, it is observed that UC has exhibited the highest Debye temperature and lattice thermal conductivity (k_L) at room temperature, while UN has the highest melting temperature. Furthermore, UC and UN have displayed the lowest thermal expansion. Overall, this extensive study on the physical properties of UX (X = C, N, O) reveals the potential application of UC and UN solid fuel materials in nuclear power plants.

Keywords: Nuclear fuels; GGA-PBE; Charge density; Elastic anisotropy; Thermal conductivity.

doi: https://dx.doi.org/10.3329/jsr.v18i1.82897 J. Sci. Res. **18** (1), 211-230 (2026)

1. Introduction

Actinide compounds, particularly uranium-based compounds, have been extensively studied due to their scientific importance in the nuclear field [1-4]. The uranium-based compounds, such as uranium carbides and nitrides, are potential nuclear fuel candidates for Generation IV reactors [5]. The most crucial thermophysical factors in the design of effective nuclear fuels for the advanced nuclear reactors are the material's melting point and thermal conductivity. Despite having a high melting point, actinide oxide fuels utilized in high-temperature nuclear reactors are not as efficient due to their poor thermal conductivity.

* *Corresponding author:* rajankarmakar15@gmail.com

On the other hand, uranium carbides [6] and uranium nitrides [1,3] have superior thermal physical properties like high melting point, high thermal conductivity, and high metal density. Because of their benefits over oxides, uranium carbides and uranium nitrides have become the scope of experimental and computational research. Amongst this group, uranium monocarbide and mononitride are two of the most important fuels.

There has been a lot of previous research on the various physical properties of solid nuclear fuels such as UC and UN, both experimentally and theoretically [1,3,6-16]. Hongliang Shi *et al*. [13] studied the electronic structures and mechanical properties of UC applying the first principle local density approximation (LDA) +U and generalized gradient approximation (GGA) + U for the exchange correlation term. They demonstrated how the electronic structures and mechanical properties of UC change with the different values of the Hubbard U parameter, and the CGA +U approximation provided the results that were close to the experimental results [13]. On the other hand, B.D. Sahoo *et al.* investigated the pressure effect up to 40 GPa on the structural properties of Uranium monocarbide using first first-principles code USPEX [14].

Additionally, in the research of Barbara Szpunar et al., they predicted the structural properties of UN using the CGA of PBE functional implemented in Quantum ESPRESSO (QE). They compared the calculated heat capacity and lattice thermal conductivity using QE and the associated code, ShengBTE, with the available experimental results [15]. Besides, the first-principles calculation software VASP has been utilized to understand the effect of vacancy defects and carbon impurities on the thermal conductivity of UN [16]. Moreover, Sahafi *et al.* [17] investigated the structural and mechanical properties of uranium monoxide theoretically. In this study, we consider uranium monoxide for comparison purposes.

However, the extensive and comparative study of structural, electronic, magnetic, vibrational, bonding, mechanical, and thermophysical properties of UC, UN, and UO has not been performed yet. The objective of this research is to fulfill this research gap using density functional theory calculations as implemented in the CASTEP code [18]. Another purpose of this investigation is to explore their suitability as a potential nuclear fuel candidate in nuclear power applications.

In this investigation, the density functional theory-based CGA-PBE [19] and CGA-PBEsol [20] functionals employed in the CASTEP code [18] have been utilized to calculate the structural properties of UX. As the structural properties calculated from the CGA-PBEsol technique exhibit better agreement with the available reference values, further calculation of electronic, magnetic, bond population, charge density, phonon spectrum, elastic, mechanical, and thermophysical characteristics of UX has been performed using the CGA-PBEsol technique. The bond population analysis and electron charge density mapping have been done to comprehend the bonding nature of the studied compound. The magnetic properties of UX compounds are also revealed by calculating the magnetic moment using the spin-polarized DFT functional in the representation of magnetic spin structure. Additionally, 3D representations of elastic moduli have been used to assess the anisotropic nature of these fuels. This research is the first time that Slack's equation [21] has been used

to compute the lattice thermal conductivity of UX (X = C, N, O) solid fuels. The swelling is another important nuclear fuel phenomenon. The growth or enlargement of fuel pellets used in nuclear reactors is referred to as "swelling of fuel materials." In this current work, we have included for the first time calculations for the thermal expansion coefficient, heat capacity (ρC_P), and wavelength of the dominant phonon (λ_{dom}) for the nuclear fuels under study.

This research paper is organized as follows: In Section 2, the computational details of this work are explained. The performed calculations and research findings are briefly presented in Section 3. Finally, the conclusion of this research is presented in Section 4.

2. Computational Method Details

In the present study, we have used the plane-wave pseudopotential approach based on the spin-polarized density functional theory (DFT) implemented in the Cambridge Serial Total Energy Package (CASTEP) to calculate the physical properties of UX (X = C, N, O) [18]. To find out the ground state of a system, the solution of the Kohn-Sham equation is applied [22]. Additionally, the generalized gradient approximation (GCA) of Perdew-Burke-Ernzerhof (PBE) [19] and PBE for solids (PBEsol) [20] have been utilized to calculate the electronic exchange-correlation energy. The PBEsol, a revised Perdew-Burke-Ernzerhof GGA tool, is used to get better results for densely packed solids. To resolve the Coulomb interaction between iron cores and valence electrons, the Vanderbilt-type ultra-soft pseudopotentials [23] are employed. The pseudo-atomic calculations are conducted for the following valence electrons: U($5f^3 6s^2 6p^6 6d^1 7s^2$), C ($2s^2 2p^2$), N ($2s^2 2p^3$), O ($2s^2 2p^4$).

To optimize the structure geometrically, the Broyden Fletcher Goldfarb Shanno (BFGS) [23] minimization technique is employed for both the GCA-PBE and GCA-PBEsol (Fig. 1). Density mixing is employed in the GGA-PBE and CGA-PBEsol models to calculate the electronic structure. During self-consistency, the total energy, the maximum ionic force, the maximum ionic displacement, and the maximum pressure are set within 1×10^{-5} eV/atom, 0.03 eV/Å, 1×10^{-3}, and 0.05 GPa, respectively. To conduct k-point sampling within the first irreducible Brillouin zone (BZ), the Monkhorst-Pack scheme [24] is used.

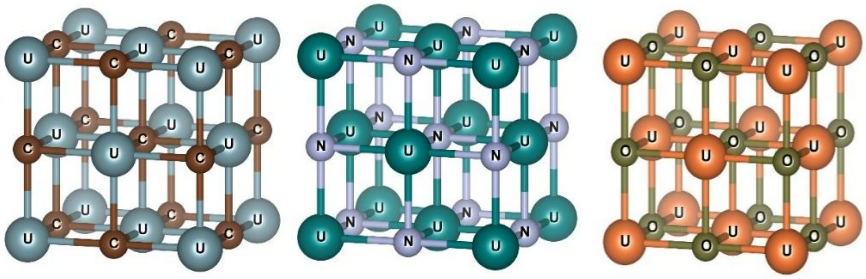

Fig. 1. The optimized 3D crystal structures of cubic UX (X = C, N, O) nuclear materials.

3. Results and Discussion

3.1. *Structural analysis*

The studied binary compounds UX (X = C, N, O) exhibit a face-centered cubic (fcc) geometric configuration of NaCl-type unit cell with a space group $Fm\bar{3}m$ (No. 225). The Wyckoff positions of atoms U and X (= C, N, O) in the unit cell of compounds are 4a (0, 0, 0) and 4b (1/2, 1/2, 1/2), respectively. Fig. 1 illustrates geometrically optimized structures of UC, UN, and UO.

Table 1 represents the estimated structural properties of UX (X = C, N, O) with other experimental and theoretical reference values. All computations from the ground state configuration have been done using the CGA-PBE and CGA-PBEsol functionals. For uranium monocarbide (UC), the calculated lattice constants are a = b = c = 5.10 Å (CGA-PBE) or a = b = c = 4.99 Å (CGA-PBEsol). The UC lattice constants a = b = c = 4.99 Å, calculated using the CGA-PBEsol functional, closely align with the experimental result [7], with a discrepancy of only 0.6%. A similar trend has been observed in the case of uranium mononitride (UN); the lattice constants, a = b = c = 4.91 Å, that are computed using the CGA-PBEsol functional, demonstrate excellent agreement with the experimental findings [8]. The difference in values is only 0.45 %. Moreover, the calculated lattice constants, a = b = c = 4.89 Å, of uranium monoxide, UO (CGA-PBEsol), are fairly close to the previously reported experimental value [26] with a 1 % discrepancy. The slight discrepancy arises due to the utilization of CGA-PBEsol and the inclusion of spin polarization [27].

Table 1. The geometrical optimized structural properties of UX (X = C, N, O).

Material	Cut-off energy (eV)	Approximation method	k-points	Lattice constant a (Å)	Volume, V ($Å^3$)	Formation Energy (eV)	Remarks
UC	600	GGA-PBE	6×6×6	5.10	129.66		This work
	500	GGA-PBEsol	6×6×6	4.99	124.79	-0.392	This work
	-	Experiment	-	4.96	-		[7]
UN	400	GGA-PBE	4×4×4	5.0	124.70		This work
	600	GGA-PBEsol	5×5×5	4.91	118.55	-1.59	This work
	-	Experiment	-	4.88	-		[8]
UO	400	GGA-PBE	8×8×8	5.0	125.37		This work
	400	GGA-PBEsol	8×8×8	4.89	117.42	-2.33	This work
	-	Exp., Theo.	-	4.94, 4.84	-		[17,26]

It is observed that lattice constants decrease from UC to UO ($C^{4-} > N^{3-} > O^{2-}$) as their anion size is smaller, and the studied lattice structures are also closely packed from UC to UO as their volume decreases. Additionally, the studied compounds, UX, are thermodynamically stable as their formation energy is negative. Their stability trend of the structure (high to low) is UO > UN > UC. Among the studied compounds, UO exhibits the smallest lattice constant and volume, and its structure is more stable compared to others. Overall, the calculated structural properties of UX (X = C, N, O) using the CGA-PBEsol exhibit good agreement with the available experimental values. So, the rest of the calculation in this paper has been performed using the CGA-PBEsol approximation functional.

3.2. *Electronic properties*

3.2.1. *Band structure*

In material science, band structure is very crucial to understanding the electrical, optical, and even magnetic properties of a crystal. The electronic band structure of the studied compounds as a function of energy ($E-E_F$) has been calculated in the first Brillouin zone along with several high symmetry directions (X - R - M - Γ - R) at zero pressure and temperature. To represent the Fermi energy (E_F), the zero-point energy is utilized in this study. From Fig. 2, we can notice that there are no band gaps at the Fermi level of UC, UN, and UO due to the overlap of valence and conduction bands, which are closely aligned with the previous finding [9-10]. However, the proportion of band overlap and crossing of the Fermi level is quite strong. Especially the intersections of bands running along Γ are more intense. This means that our studied compound UX (X = C, N, O) will exhibit a metallic character.

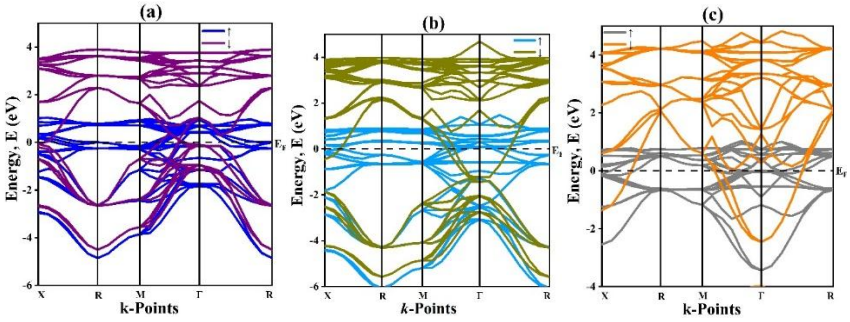

Fig. 2. The electronic band structures of cubic (a) UC, (b) UN, and (c) UO nuclear materials.

3.2.2. *Density of states*

The computed total density of states (TDOS) and partial density of states (PDOS) of UC, UN, and UO at zero temperature and pressure are presented in Fig. 3, respectively. The vertical broken lines represent the Fermi level, while the horizontal broken lines act as a

boundary between up and down spins. The partial density of the state is very important in understanding each atom's role in the TDOS. For all compounds, the values of TDOS are nonzero at the Fermi level, which indicates their metallic electrical conductivity. Near the Fermi level, the major contribution comes from U-5f, and the minor contributions arise from U-6d and C/N/O-2p in UC, UN, and UO. Due to the hybridization among uranium 5f and 6d orbitals, and carbon/nitrogen/oxygen 2p orbitals, there is a degree of covalent bonds in UX (X = C, N, O). A high contribution in PDOS from uranium orbitals expresses polarity in the bond.

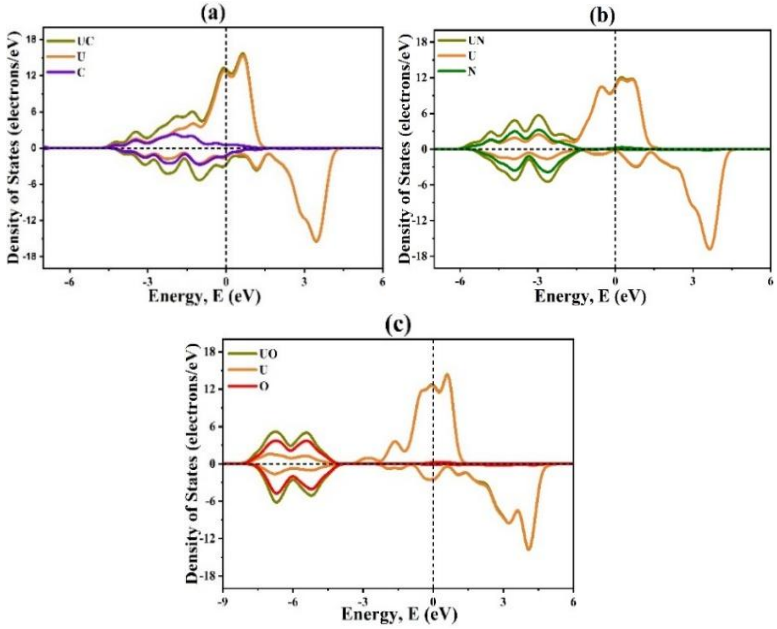

Fig. 3. The total and partial (a) DOS of UC, (b) DOS of UN, and (c) DOS of UO materials.

The DOS curves also help to assess the magnetic behavior of compounds and their magnetic moment per formula unit. The magnetic properties of solid nuclear fuels are very crucial because magnetic ordering can manipulate the fuel's behavior under extreme conditions. We have calculated the magnetic moments per formula unit by using equation [27]:

$$\text{Magnetic Moment, } \mu = \frac{\text{Integrated spin up value at Fermi level-Integrated spin down value at Fermi level}}{\text{Number of formula units (f.u.) per unit cell}}$$

The calculated values of the magnetic moment per formula unit can be found in Table 2. The magnetic moment values of UC and UO are comparable, while the value of the magnetic moment of UN is the lowest. Fig. 3 shows that the magnetic moment mainly emerges from the U atoms in the UX (X = C, N, O) compounds.

Table 2. The estimated (CGA-PBEsol) and available reference values of structural, electronic, and magnetic parameters of UX (X = C, N, O).

Compound	Band gap, E_g (eV)	No. of atoms per unit cell	No. of formula units (f.u.) per unit cell	Magnetic moment, μ (μ_B/f.u.)	Remarks
UC	0.00	8	4	3.84	This work
	0.00	-	-	-	[9]
UN	0.00	8	4	2.75	This work
	0.00	-	-	-	[10]
UO	0.00	8	4	3.81	This work

3.3. *Phonon dynamics*

The calculated phonon dispersion curves of UX, presented in Fig. 4, serve as a key indicator to evaluate their dynamical stability. The presented figures of phonon spectra have been drawn in high-symmetry directions of the Brillouin zone and accompanied by the total density of phonon states on the right. From the figures, it is observed that UC, UN, and UO are dynamically stable as they have no imaginary frequencies in their spectra.

In Figs. 4a-c, the blue color curves represent the acoustic branches, whereas the purple color curves represent the optical branches. As a unit cell of the studied compounds has 8 atoms, there are a total of 24 phonon modes (3 acoustic modes and 21 optical modes). Additionally, there is no separation gap between optical and acoustic modes in the lower frequency region of the compounds, which indicates that there is significant coupling between uranium and C/N/O atoms. However, there are two optical branches in the phonon spectrum, one is situated in the lower optical region (3-4 THz), while the other is situated in the upper optical region (10-12 THz). From the graph, it is observed that the acoustic mode becomes zero frequency at the Γ-point, which also confirms the compound's dynamical stability.

On the other hand, the total density of phonon states exhibits a continuous distribution of states without any anomaly, which confirms these findings about the stability. Overall, the phonon spectrum of UX suggests that the studied structures are dynamically stable.

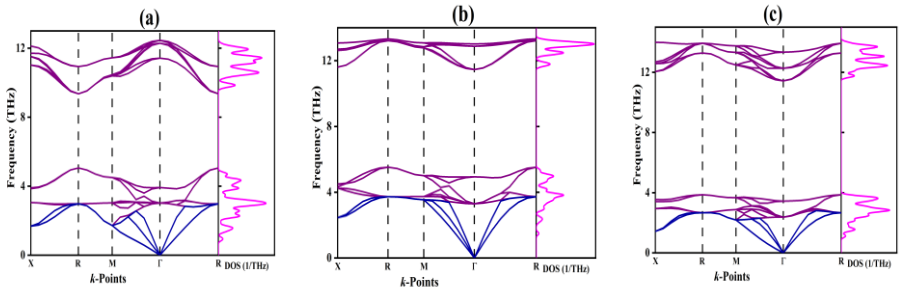

Fig. 4. The phonon dispersion curves of (a) UC, (b) UN, and (c) UO.

3.4. *Bond population analysis*

The Mulliken bond populations are calculated to understand the bonding nature (ionic, covalent, or metallic) and effective valence of an atom in the molecule in detail [28]. The results of these findings for UX (X = C, N, O) are listed in Table 3. The charge spilling parameters of UX are lower, indicating that the electronic bond is strong. From Table 3, we have noticed that atomic charges for U and X (= C, N, O) atoms in UX (X = C, N, O) have deviated from the purely ionic state of U and X (= C, N, O), which reflects the presence of some covalent bonding character in UX (X = C, N, O). Due to the electron transfer from U to X, one can anticipate that an ionic bond dominates between U and X (= C, N, O) in UX.

Table 3. The calculated charge spilling parameter (%), orbital charges (electron), atomic Mulliken charges (electron), effective valence (electron), and Hirshfeld charge (electron) UX (X = C, N, O).

M	CP	E	s	p	d	f	T	MC	FIC	EV	HC	EV
UC	0.6	U	2.28	5.90	2.47	2.72	13.37	0.63	+3	2.37	0.34	2.66
		C	1.51	3.12	0	0	4.63	-0.63	0	0.63	-0.34	0.34
UN	0.08	U	2.26	6.01	2.18	2.88	13.33	0.67	+3	2.33	0.34	2.66
		N	1.70	3.97	0	0	5.57	-0.67	-3	2.33	-0.34	2.66
UO	0.12	U	2.33	6.01	1.99	3.17	13.43	0.57	+3	2.43	0.25	2.75
		O	1.84	4.73	0	0	6.57	-0.57	-2	1.43	-0.25	1.75

Note: M = Material; CP =Chage Spilling; E = Element; T = Total; MC= Muliken Charge; FIC= Formal Ionic Charge; EV= Effective Valence; HC= Hirshfeld Charge; Orbital = s, p, d, f.

The distinction between the formal ionic charge and the Mulliken charge on the cation species in the crystal is known as effective valence [29]. The effective valence of UX is computed to determine the degree of covalency and/or iconicity. An ionic bond is perfect when the effective valence value is zero, while values greater than zero indicate a higher level of covalency. In UX, the effective valences of U are positive. This suggests that UX (X = C, N, O) has both covalent and ionic bonds.

Sometimes, the Mulliken bond population analysis gives incorrect results for its sensitivity to the chosen atomic basis set, but the Hirshfeld population analysis (HPA) [30] provides us with more meaningful results by eliminating the need for a basis set reference or its location. So, we have calculated the Hirshfeld charge of U and X (= C, N, O) atoms in UX. However, the findings exhibit the same result as we have achieved from the Mulliken charge. We have also computed the effective valences from the Hirschfeld charges. Similar result, we have found that UX (X = C, N, O) has both covalent and ionic bonds.

Table 4. The estimated Mulliken bond number n^{μ}, bond overlap population P^{μ}, and bond length d^{μ} of UX (X = C, N, O).

Material	Bond	n^{μ}	P^{μ}	d^{μ}
UC	C-U	12	0.48	2.4986
UN	N-U	12	0.39	2.4562
UO	O-U	12	0.25	2.4483

Table 4 represents the calculated Mulliken bond number, bond overlap population, and bond length of UX (X = C, N, O). The number of bonds is the same for all of the studied compounds. In addition, the C-U bond length is higher than the N-U and O-U bond lengths. Mulliken bond populations in a crystal determine the degree of electron cloud overlap between two bonding atoms. The covalent bond strength between atoms and the bond strength per unit volume are determined by bond order, which quantifies the overlap of the electron population. The estimated bond overlap population of UX is positive. As the bond overlap population is higher in UC than in UN and UO, this indicates that covalent bonding-type interaction dominates in UC.

3.5. *Electronic Charge Density*

To get further information about the bonding nature of our studied compounds, we have studied the electronic charge density of UX (X = C, N, O). The electronic charge density maps are illustrated in Fig. 5 with colored scales on the right. From the maps, we can notice that U atoms have a high electronic charge density compared to C and N atoms in UC and UN. In contrast, the O atom has a high electronic charge density compared to the U atom in UO. Therefore, the domination of ionic bonds is expected in UN and UO, while a covalent bond dominates in UC. This agrees with the result we have obtained from the bond population analysis.

3.6. *Elasto-Mechanical Properties*

The second-order elastic stiffness constants (C_{ij}) of the material are crucial for material selection, comprehending how materials respond to mechanical forces, anticipating distortion, and material nature, etc. The elastic properties play essential roles throughout the years [31,32] in engineering, condensed matter physics, materials science, geophysics, and chemistry. The cubic solid nuclear fuels have three independent elastic constants: C_{11}, C_{12}, and C_{44}. This happens because of crystal symmetry $C_{11} = C_{22} = C_{33}$, $C_{12} = C_{23} = C_{13}$ and $C_{44} = C_{55} = C_{66}$. The computed and available reference values of C_{ij} of UX from the CGA-PBEsol approximation are presented in Table 5. The previously reported elastic constants of UC [11] and UN [12] are fairly close to the calculated C_{ij} of UC and UN. It is not possible to compare the elastic constants of UO due to the lack of reference values. The famous Born stability conditions [33], which are used to examine the mechanical stability of cubic crystals, are mentioned below.

$$C_{11} - C_{12} > 0,\ C_{11} + 2C_{12} > 0,\ C_{44} > 0 \quad (1)$$

All of our studied compounds are mechanically stable, as the Born stability criterion of UC, UN, and UO is fulfilled. C_{44} parameterizes a compound's resistance to shear deformation in the [010] direction with respect to a tangential force applied across the (100) plane. UX is more readily deformed by a shear than by a unidirectional compression along any of the three crystallographic orientations, as can be observed here, as C_{44} is lower than C_{11}.

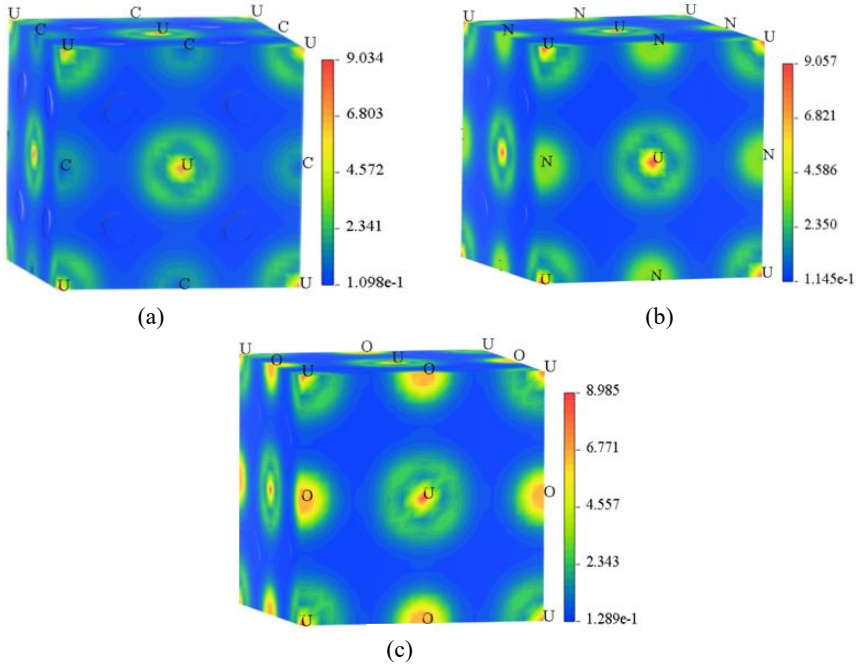

Fig. 5. The electronic charge density distribution 3D maps of (a) UC, (b) UN, and (c) UO.

The Hill's formalism [34], which is the average of Voigt [35] and Reuss [36] approximations, has been utilized to compute bulk modulus (B), shear modulus (G), and Young's modulus (Y).

$$B = \frac{B_V + B_R}{2} \tag{2}$$

$$\text{where, } B_V = \frac{2(C_{11} + C_{12}) + C_{33} + 4C_{13}}{9} \text{ and } B_R = \frac{(C_{11} + C_{12})C_{33} - 2C_{13}^2}{C_{11} + C_{12} + 2C_{33} - 4C_{13}}$$

B_V and B_R represent the Voigt and Reuss bulk moduli, respectively. Similarly:

$$G = \frac{G_V + G_R}{2} \tag{3}$$

$$\text{where, } G_V = \frac{C_{11} + C_{12} + 2C_{33} - 4C_{13} + 12C_{44} + 12C_{66}}{9} \text{ and } G_R = \frac{\frac{5}{2}[(C_{11} + C_{12})C_{33} - 2C_{13}^2]C_{44}C_{66}}{3B_V C_{44}C_{66} + [(C_{11} + C_{12})C_{33} - 2C_{13}^2](C_{44} + C_{66})}$$

G_V and G_R represent the Voigt and Reuss shear moduli, respectively.

After that, the Young's modulus (Y) and Poisson's ratio (σ) are computed utilizing the values of B and G by the following equation [37]:

$$Y = \frac{9BG}{3B+G} \quad \text{and} \quad \sigma = \frac{3B-2G}{2(3B+G)} \tag{4}$$

Table 5. The estimated and the available reference values of elastic constants C_{ij} (GPa), bulk modulus B (GPa), shear modulus G (GPa), Young's modulus Y (GPa) of solid nuclear fuel material UX (X = C, N, O).

Material	C_{11}	C_{12}	C_{44}	B	G	Y	Remarks
UC	335.77	81.75	55.61	166.42	77.96	202.28	This work
	315	77	61	158	-	-	[10]
UN	382.30	111.15	50.82	201.53	76.23	203.11	This work
	423	98.10	75.7	205.9	103.9	229	[11]
UO	350.16	49.23	22.32	149.54	53.72	143.92	This work

All of the computed values of B, G, and Y with the previously reported values are presented in Table 5. And the calculated values of elastic moduli are well aligned with the available reference values [11,12] for UC and UN, respectively. A greater value of B relative to G (Table 5) suggests that shear modulus will dominate mechanical stability. Moreover, in this study, the Cauchy pressure ($C'' = C_{12} - C_{44}$), Poisson's ratio (σ), Pugh's ratio (B/G), and machinability index (B/C_{44}) are also calculated and listed in Table 6.

Table 6. The estimated mechanical parameters of solid nuclear fuel material UX (X = C, N, O).

Material	C″ (GPa)	σ	B/G	B/C_{44}	Nature	Remarks
UC	26.14	0.297	2.14	2.99	Ductile	This work
	16	-	-	-	Ductile	[11]
UN	60.33	0.332	2.64	3.97	Ductile	This work
	22.4	0.263	-	-	Ductile	[12]
UO	26.91	0.339	2.78	6.69	Ductile	This work

The Pugh's ratio, Poisson's ratio, and machinability index of UC, UN, and UO are illustrated in Fig. 6. Solid materials whose Poisson's and Pugh's ratios are less than 0.26 and 1.75, respectively, are considered brittle, according to reference [38]. Furthermore, when the value of the Cauchy pressure is positive or negative, the material is assumed, respectively, as a ductile or brittle solid [38]. From Table 6, it becomes clear that all the studied solid nuclear fuels are mechanically ductile. UO exhibits the highest ductility compared to UC and UN. In addition, UO is easier to work with in terms of cutting or machining processes, as its machinability index is the highest.

The Vickers hardness (H_V) is a crucial parameter for understanding the mechanical performance of a material. There are different reliable empirical formulas [39-43] to estimate the Vickers hardness. The used formalisms are:

$$(H_V)_{Teter} = 0.151G \tag{5}$$

$$(H_V)_{Chen} = 2\left(\frac{G^3}{B^2}\right)^{0.585} - 3 \tag{6}$$

$$(H_V)_{Miao} = \frac{(1-2\sigma)Y}{6(1+\sigma)} \tag{7}$$

$$(H_V)_{Tian} = 0.92\left(\frac{G}{B}\right)^{1.137} G^{0.708} \tag{8}$$

$$(H_V)_{Mazhnik} = \gamma_0\, \chi(\sigma)\, Y \tag{9}$$

$$\text{where, } \chi(\sigma) = \frac{1 - 8.5\sigma + 19.5\sigma^2}{1 - 7.5\sigma + 12.2\,\sigma^2 + 19.6\sigma^3}$$

*γ_0 = 0.096 (dimensionless constant)

The calculated Vickers hardness of the studied compounds using different models (Teter, Chen, Miao, Tian, Mazhnik) has been presented in Table 7 and illustrated in Fig. 6. All of the model except Mazhnik shows that UC exhibits the highest hardness, followed by UN and UO. This indicates that UC is mechanically stronger than others. The output from Mazhnik shows that UN is harder than UC. This may happen due to the model sensitivity.

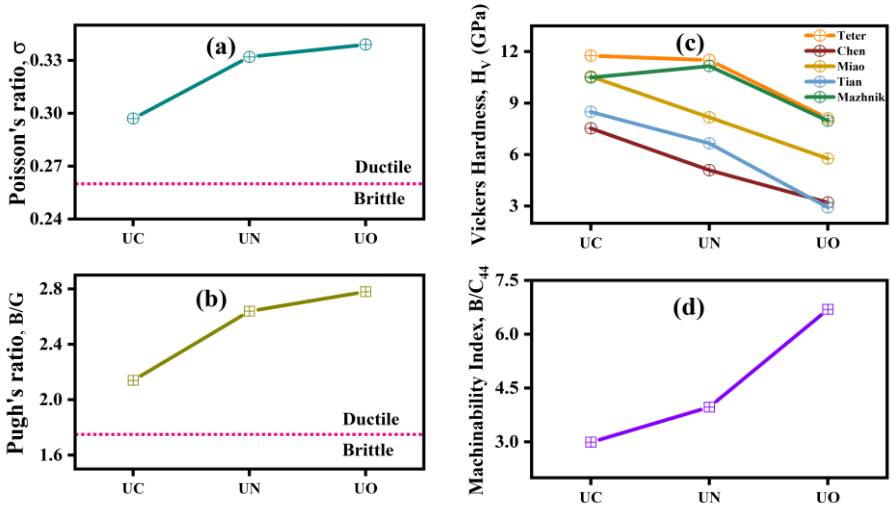

Fig. 6. (a) Pugh's ratio (B/G), (b) Poisson's ratio (ρ), (c) Vickers Hardness (HV), and (d) Machinability index (B/C_{44}) diagrams of UX (X = C, N, O).

The Teter model provides the highest values of Vickers hardness of UX as it is directly linked with the shear modulus. On the other hand, Chen's model gives the lowest values of hardness for UC and UN, in contrast to Tian's model, which provides the lowest values of hardness for UO.

Table 7. The estimated Vickers hardness values of solid nuclear fuel material UX (X = C, N, O) using different empirical formulas.

Material	$(H_V)_{Teter}$	$(H_V)_{Chen}$	$(H_V)_{Miao}$	$(H_V)_{Tian}$	$(H_V)_{Mazhnik}$
UC	11.77	7.53	10.55	8.49	10.49
UN	11.51	5.09	8.17	6.66	11.16
UO	8.11	3.21	5.77	2.92	7.97

3.6.1. *Anisotropy*

To understand the anisotropic nature of a compound, elastic Anisotropy is an important tool to assess asymmetry in the atomic arrangement in the different crystal directions, such as xy, xz, and yz. That's why the Zener anisotropy and Universal anisotropy factor for ThX have been estimated. To estimate the Zener anisotropy (A) and Universal anisotropy factor (A^U) [44], the mentioned equations have been used:

$$\text{Zener anisotropy,} \qquad A = \frac{2C_{44}}{C_{11} - C_{12}} \tag{10}$$

$$\text{Universal anisotropy factor,} \qquad A^U = 5\frac{G_V}{G_R} - 5 \geq 0 \tag{11}$$

A material will be an isotropic material if the values of A and A^U are within 1 and 0, respectively [45]. The calculated values of the Zener anisotropy and Universal anisotropy factor are presented in Table 8. From the table, it is overserved that the UO shows the most anisotropic structure among others. Both factors, A and A^U exhibit the following anisotropic trend: UC (least) < UN (intermediate) < UO (highest).

Table 8. The calculated Zener anisotropy index (A) and Universal anisotropy index (A^U) of UX.

Material	Zener anisotropy (A)	Universal anisotropy factor (A^U)
UC	0.438	0.866
UN	0.375	1.251
UO	0.148	1.862

To visualize the elastic anisotropy characteristics of UX (X = C, N, O), the 3D of Young's modulus (Y), shear modulus (G), and Poisson's ratio σ are presented in Fig. 7, which are generated by the ELATE tool [46]. All of the plots clearly show deviation from spherical symmetry, which indicates that the studied compounds exhibit elastic anisotropy. Table 7 represents the upper and lower limits of Y, G, and σ of UX (X = C, N, O).

3.7. *Thermophysical Properties*

To comprehend the thermal stability of material under high temperature, the thermal parameters such as Debye temperature (Θ_D), melting temperature (T_m), minimum thermal conductivity (k_{min}), and lattice thermal conductivity (k_L) are very essential. Elastic constants can be used to calculate these parameters. We have utilized the famous Anderson method [47] to calculate the Debye temperature, (Θ_D), which is given in the following equation:

$$\Theta_D = \frac{v_m h}{k_B}\left[\frac{3n}{4\pi}\frac{N_A \rho}{M}\right]^{\frac{1}{3}} \tag{12}$$

where h, k_B, n, N_A, ρ, M, and v_m denote Planck's constant, the Boltzmann constant, the number of atoms per molecule (2), the Avogadro's number, the mass density, the molecular weight, and the average acoustic velocity respectively. v_m can be calculated from the following relation:

$$v_m = \left[\frac{1}{3}\left(\frac{2}{v_t^3} + \frac{1}{v_l^3}\right)\right]^{-\frac{1}{3}} \tag{13}$$

where v_t and v_l represent, respectively, the transverse and longitudinal acoustic velocities. v_t and v_l are computed from Shear and Bulk moduli using Navier's equations [47]:

$$v_l = \left(\frac{3B + 4G}{3\rho}\right)^{\frac{1}{2}} \quad \text{and} \quad v_t = \left(\frac{G}{\rho}\right)^{\frac{1}{2}} \tag{14}$$

The Debye temperature (Θ_D) is an important parameter to understand the thermal transport behavior of a material. The calculated Debye temperatures for UC, UN, and UO are summarized in Table 10. UC exhibits the highest Debye temperature (326.69), followed by UN at 313.97 K, UO at 263 K. The higher value of Θ_D for UC suggests that UC will show excellent lattice stability under extreme conditions like a nuclear fuel environment. The importance to the UN is also noteworthy, confirming its standing as a promising contender for applications involving advanced nuclear fuel.

Compound	Young's modulus (Y)	Shear modulus (G)	Poisson's ratio (σ)
UC	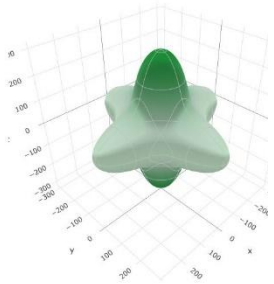	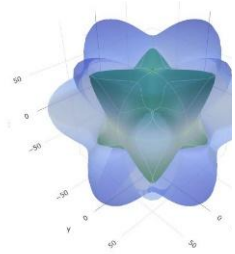	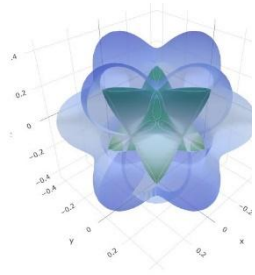
UN	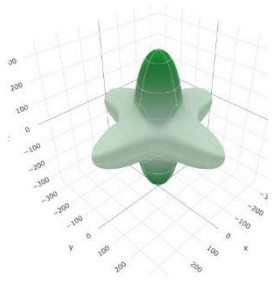	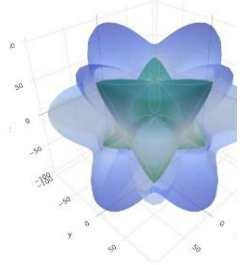	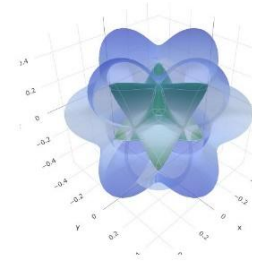

Uo

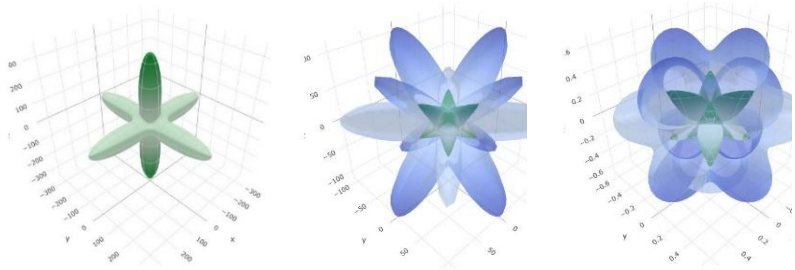

Fig. 7. The anisotropic 3D presentations of Young's modulus, Shear modulus, and Poisson's ratio of UC, UN, and UO.

Table 9. The lower and upper limit of Young's Modulus (Y), Shear Modulus (G), and Poisson's ratio (σ) of UX (X = C, N, O).

Material	Young's Modulus (GPa)			Shear Modulus (GPa)			Poisson's ratio		
	Y_{min}	Y_{max}	Anisotropy	G_{min}	G_{max}	Anisotropy	σ_{min}	σ_{max}	Anisotropy
UC	150.11	303.76	2.02	55.61	127.01	2.28	0.111	0.545	4.92
UN	140.63	332.22	2.36	50.82	135.57	2.67	0.111	0.617	5.54
UO	63.79	338.02	5.29	22.32	150.46	6.74	0.029	0.793	27.16

The relation mentioned [48] below can be used to calculate the minimum thermal conductivity, k_{min}:

$$k_{min} = k_B v_s \left(\frac{M}{n\rho N_A}\right)^{-\frac{2}{3}} \quad (15)$$

The lattice thermal conductivity, k_L of UX (X = C, N, O) has been evaluated by the famous Slack's formula [21]:

$$k_L = A(\gamma)\frac{M_{av}\,\theta_D{}^3\,\delta}{\gamma^2\, n^{\frac{2}{3}} T} \quad (16)$$

where, δ, M_{av}, n, T, γ, and A refer to the cubic root of the average atomic volume, the average atomic mass in kg/mole (M_{av} = M/n, where n is the number of atoms in the molecule) in a crystal, the number of atoms in a unit cell, the absolute temperature in K, the Grüneisen parameter obtained from Poison's ratio (σ), and a γ dependent constant respectively. The Grüneisen parameter γ and the factor A can be calculated as [27]:

$$\gamma = \frac{3(1+\sigma)}{2(2-3\sigma)} \quad \text{and} \quad A(\gamma) = \frac{2.43 \times 10^7}{1 - \frac{0.514}{\gamma} + \frac{0.228}{\gamma^2}} \quad (17)$$

The computed values of the parameters δ, γ, ρ, v_m, A, Θ_D, k_{min}, k_L (at 300 K) are tabulated in Table 10. Since thermal transport directly controls heat dissipation at high power densities, it is an essential metric for assessing a material's effectiveness as a nuclear fuel. UC's minimum thermal conductivity (k_{min}) is 0.601 $Wm^{-1}K^{-1}$, UN's is 0.596 $Wm^{-1}K^{-1}$, and UO's is 0.499 $Wm^{-1}K^{-1}$. Even though the differences seem slight, they are consistent with the behavior predicted by the γ and v_m trends, demonstrating that UC and UN have a higher thermal transfer capacity than UO.

In addition, the variation of lattice thermal conductivity as a function of temperature is illustrated in Fig. 8. From Fig. 8, we can observe that the value of the lattice thermal conductivity of UC is the highest compared to UN, and UO. At room temperature, k_L value of UC is 9.35 $Wm^{-1}K^{-1}$, while k_L values of UN and UO are 6.14 $Wm^{-1}K^{-1}$ and 4.03 $Wm^{-1}K^{-1,}$ respectively. The calculated thermal lattice conductivity of UN is fairly close to the previously reported value [49]. However, it is not possible to verify the k_L values of UC and UO due to the lack of available reference values.

Table 10. The estimated cubic root of average atomic volume (δ), Grüneisen parameter (γ), mass density (ρ), average acoustic velocity (v_m), constant (A), Debye temperature (Θ_D), minimum thermal conductivity (k_{min}), and lattice thermal conductivity (k_L) of UX (X = C, N, O) materials.

Material	δ (Å)	γ	ρ (gm/cm^3)	v_m (km/s)	A × 10^7	Θ_D (K)	k_{min} ($Wm^{-1}K^{-1}$)	k_L ($Wm^{-1}K^{-1}$)	Remarks
UC	2.49	1.75	14.21	2.60	3.16	326.69	0.601	9.35	This work
UN	2.46	2.03	14.12	2.59	3.17	313.97	0.596	6.14	This work
	-	-	-	-	-	282 [11]	-	7.25 [49]	
UO	2.445	2.04	14.37	2.17	3.51	263	0.499	4.03	This work

The melting temperature, T_m has a direct relationship with the elastic constants. T_m for cubic crystals can be computed by the following empirical formula [50]:

$$T_m = 553 + 5.91C_{11} \pm 300 \quad (18)$$

The calculated melting temperature of UX is presented in Table 11, where UN exhibits the highest melting temperature. The thermal expansion coefficient has a significant relation with various other physical properties such as specific heat, melting point, thermal conductivity, and the temperature-dependent characteristics of the energy band gap in semiconductors. The thermal expansion coefficient (α) is calculated by the following equation [27]:

$$\alpha = \frac{1.6 \times 10^{-3}}{G} \quad (19)$$

The calculated values of α has been listed in Table 11. From the table, we can observe that UC and UN exhibit the minimal thermal expansion compared to UO.

The heat capacity is an important thermodynamic property of a material. The change in thermal energy per unit volume of a compound for each degree Kelvin of temperature change is known as the heat capacity per unit volume ρC_P. It is possible to determine a material's heat capacity per unit volume by employing the method outlined below [27]:

$$\rho C_P = \frac{3k_B}{\Omega} \quad (20)$$

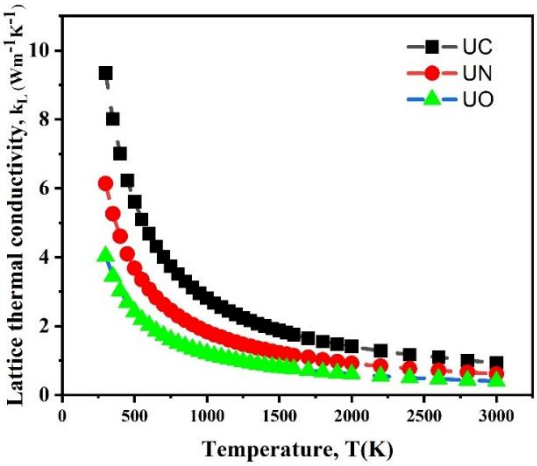

Fig. 8. The variation of lattice thermal conductivity (K_L) of UX (X = C, N, O) as a function of temperature.

The calculated heat capacities per unit volume of UX are presented in Table 11. The heat capacity values of UC, UN, and UO are very close to each other.

Table 11. The estimated melting temperature (T_m), thermal expansion coefficient (α), heat capacity per unit volume (ρC_P) and dominant phonon wavelength (λ_{dom}).

Material	$T_m \pm 300$ (K)	$\alpha \times 10^{-5}$ (K^{-1})	$\rho C_P \times 10^6$ ($JK^{-1}m^{-3}$)	$\lambda_{dom} \times 10^{-12}$ m (at 300 K)	Remarks
UC	2537.40	2.05	2.65	108.91	This work
UN	2812.39	2.10	2.79	108.49	This work
	2923 ±100	-	-	-	[12]
UO	2622.45	2.97	2.82	90.89	This work

It is crucial that phonons play a part in identifying the various physical characteristics that solid materials exhibit. The peak of the phonon distribution function is reached by the dominant phonon's wavelength, or λ_{dom}. The dominant phonon's wavelength λ_{dom} for UX materials at room temperature (T = 300 K) has been calculated using the provided equation.

$$\lambda_{dom} = \frac{12.566 v_m}{T} \times 10^{-12} \quad (21)$$

A compound with a higher shear modulus, lower density, and larger v_m exhibits a correspondingly higher λ_{dom}. In Table 11, the computed results for λ_{dom} are given. Overall, it can be concluded that UC and UN have the necessary thermophysical characteristics as potential nuclear fuels for the advanced nuclear reactor compared to UO due to their superior thermal conductivity and higher Debye temperatures. Their efficient heat dissipation capacity due to the higher thermal conductivity, makes them suitable for high burn-up and fast reactor systems.

4. Conclusion

In this research, the first principle study-based CASTEP code has been utilized to investigate the physical properties of UX (X = C, N, O). The geometrization of the studied unit cells is done through the PBE and PBEsol parameterized CGA exchange-correlation functional. Notably, the optimized lattice parameters of UX obtained from the CGA-PBEsol functional method have aligned well with the previously reported experimental values compared to the CGA-PBE functional. The computational efficiency of the CGA-PBEsol functional to get the geometrically relaxed unit cell structure of UX is observed over the CGA-PBE functional. So, the further study of structural, electronic, magnetic, bond analysis, electron charge density, elasto-mechanical, and thermal properties has been performed using the CGA-PBEsol method. The calculated electronic band structures of our studied compounds exhibit metallic nature, which are supported by the previously reported results. The calculated formation energy and phonon spectrum diagrams of UC, UN, and UO suggest that the studied compounds are thermodynamically stable. From the bond population analysis, the admixture of ionic and covalent bonds in UX has been revealed. All of the studied materials are elastically and mechanically stable, while the calculated values of Poisson's ratio (σ), Cauchy pressure (C") and Pugh's ratio (B/G) have indicated that UX are ductile. Additionally, the elastic anisotropy of UC, UN, and UO has been confirmed from the 3D plot of elastic moduli. UC has displayed the highest Debye temperature (Θ_D) and the lattice thermal conductivity (k_L) at 300K among other nuclear fuels, while UN has exhibited the highest melting temperature. The thermophysical analysis also suggests that UC and UN exhibit minimal thermal expansion, and all of the materials have comparable heat capacity. All of these outcomes underscore that UC and UN compounds are potential nuclear fuel candidates for particularly in fast breeder reactors and Generation-IV systems. Their favorable thermal properties also support their application in aerospace, extreme environments etc.

References

1. L. R. Morss, N. M. Edelstein, J. Fuger, and J. J. Katz, The Chemistry of the Actinide and Transactinide Elements (Springer, New York, 2006) **1**.
2. M. Stan, J. C. Ramirez, P. Cristea, S. Y. Hu, C. Deo, B. P. Uberuaga, S. Srivilliputhur, S. P. Rudin, and J. M. Wills, J. Alloys Compd. **444**, 415 (2007). https://doi.org/10.1016/j.jallcom.2007.01.102
3. International Nuclear Society Council (INSC), A Vision for the Second 50 Years of Nuclear Energy, Technical Report (American Nuclear Society, 1996.
4. M. Islam, J. Sci. Res. **15**, 739 (2023). https://doi.org/10.3329/jsr.v15i3.64394
5. D. Butler, Nature **429**, 238 (2004). https://doi.org/10.1038/429238a
6. B. Szpunar, J. A. Szpunar, Int. J. Nucl. Energy **2014**, ID 178360 (2014). https://doi.org/10.1155/2014/178360
7. H. Matsui, K. I. Sakanishi, M. Inagaki, H. Aoyama, and T. Kirihara, J. Nucl. Mater. **57**, 93 (1975). https://doi.org/10.1016/0022-3115(75)90182-8
8. E. H. P. Cordfunke, J. Nucl. Mater. **56**, 319 (1975). https://doi.org/10.1016/0022-3115(75)90049-5

9. J. Pandya, P. D. Patel, S. Shinde, S. D. Gupta, and P. K. Jha, Mater. Today: Proc. **47**, 571 (2021). https://doi.org/10.1016/j.matpr.2020.10.657
10. P. Modak and A. K. Verma, Phys. Rev. B **84**, ID 024108 (2011). https://doi.org/10.1103/PhysRevB.84.024108
11. W. J. L. Buyers, T. M. Holden, Handbook on the Physics and Chemistry of the Actinides **2**, 239 (1985).
12. M. D. Salleh, J. E. MacDonald, G. A. Saunders, and P. D. V. D. Plessis, J. Mater. Sci. **21**, 2577 (1986). https://doi.org/10.1007/BF01114310
13. H. Shi, P. Zhang, S. S. Li, B. Sun, and B. Wang, Phys. Lett. A **373**, 3577 (2009). https://doi.org/10.1016/j.physleta.2009.07.074
14. B. D. Sahoo, K. D. Joshi, and T. C. Kaushik, Comput. Condens. Matter **21**, ID e00431 (2019). https://doi.org/10.1016/j.cocom.2019.e00431
15. B. Szpunar, J. I. Ranasinghe, L. Malakkal, and J. A. Szpunar, J. Alloys Compd. **879**, ID 160467 (2021). https://doi.org/10.1016/j.jallcom.2021.160467
16. Y. Lan, T. Rui, Z. Ma, L. Lu, Y. Wang, and Y. Yu et al., Crystals **15**, 459 (2025). https://doi.org/10.3390/cryst15050459
17. M. H. Sahafi and E. Cholaki, J. Nucl. Res. Appl. **3**, 1 (2023). https://doi.org/10.24200/jon.2023.1070
18. S. J. Clark, M. D. Segall, C. J. Pickard, P. J. Hasnip, M. J. Probert, K. Refson, and M. C. Payne, Z. Kristallogr. **220**, 567 (2005). https://doi.org/10.1524/zkri.220.5.567.65075
19. J. P. Perdew, K. Burke, and M. Ernzerhof, Phys. Rev. Lett. **77**, 3865 (1996). https://doi.org/10.1103/PhysRevLett.77.3865
20. J. P. Perdew, A. Ruzsinszky, G. I. Csonka, O. A. Vydrov, G. E. Scuseria, L. A. Constantin, X. Zhou, and K. Burke, Phys. Rev. Lett. **100**, ID 136406 (2008). https://doi.org/10.1103/PhysRevLett.100.136406
21. D. T. Morelli, and G. A. Slack, in High Thermal Conductivity Materials, ed. S. L. Shindé et al., (Springer, New York, 2006). https://doi.org/10.1007/0-387-25100-6_2
22. W. Kohn and L. J. Sham, Phys. Rev. **140**, ID A1133 (1965). https://doi.org/10.1103/PhysRev.140.A1133
23. J. S. Lin, A. Qteish, M. C. Payne, V. V. Heine, Phys. Rev. B **47**, ID 4174 (1993). https://doi.org/10.1103/PhysRevB.47.4174
24. R. Fletcher, Practical Methods of Optimization, 2nd Edition (John Wiley and Sons, New York, 1987).
25. J. D. Pack, H. J. Monkhorst, J. Phys. Condens. Matter **16**, ID 1748 (1977). https://doi.org/10.1103/PhysRevB.16.1748
26. F. A. Wedgwood, J. Phys. C: Solid State Phys. **7**, 3203 (1974). https://doi.org/10.1088/0022-3719/7/18/006
27. M. Islam, Chem. Phys. **7**, ID 100310 (2023). https://doi.org/10.1016/j.chphi.2023.100310
28. R. S. Mulliken, J. Chem. Phys. **23**, 1833 (1955). https://doi.org/10.1063/1.1740588
29. M. D. Segall, R. Shah, C. J. Pickard, and M. C. Payne, Phys. Rev. B **54**, ID 16317 (1996). https://doi.org/10.1103/PhysRevB.54.16317
30. F. L. Hirshfeld, Theor. Chim. Acta **44**, 129 (1977). https://doi.org/10.1007/BF00549096
31. T. Lay and T. C. Wallace, Modern Global Seismology (Elsevier, 1995) **58**.
32. C. H. Turner, S. C. Cowin, J. Y. Rho, R. B. Ashman, and J. C. Rice, J. Biomech. **23**, 549 (1990). https://doi.org/10.1016/0021-9290(90)90048-8
33. M. Born, Math. Proc. Camb. Philos. Soc. **36**, 160 (2008). https://doi.org/10.1017/s0305004100017138
34. R. Hill, Proc. Phys. Soc. A **65**, 349 (1952). https://doi.org/10.1088/0370-1298/65/5/307
35. W. Voigt, Lehrbuch der Kristallphysik (Teubner, Leipzig, 1928).
36. A. Reus, ZAMM **9**, 49 (1929). https://doi.org/10.1002/zamm.19290090104
37. M. A. Ali, M. W. Qureshi, Vacuum **201**, ID 111072 (2022). https://doi.org/10.1016/j.vacuum.2022.111072

38. M. Islam and M. A. R. Sheikh, Phys. B: Cond. Matter **668**, ID 415244 (2023). https://doi.org/10.1016/j.physb.2023.415244
39. D. M. Teter, MRS Bulletin **23**, 22 (1998). https://doi.org/10.1557/S0883769400031420
40. X. Q. Chen, H. Niu, D. Li, and Y. Li, Intermetallics **19**, 1275 (2011). https://doi.org/10.1016/j.intermet.2011.03.026
41. N. Miao, B. Sa, J. Zhou, and Z. Sun, Comput. Mater. Sci. **50**, 1559 (2011). https://doi.org/10.1016/j.commatsci.2010.12.015
42. Y. Tian, B. Xu, and Z. Zhao, Int. J. Refract.Metals Hard Mater. **33**, 93 (2012). https://doi.org/10.1016/j.ijrmhm.2012.02.021
43. E. Mazhnik and A. R. Oganov, J. Appl. Phys. **126**, 12 (2019). https://doi.org/10.1063/1.5113622
44. C. M. Kube, Elastic anisotropy of crystals, AIP Adv. **6**, ID 095209 (2016). https://doiorg/10.1063/1.4962996
45. F. Mouhat, F. X. Coudert, Phys. Rev. B **90**, ID 224104 (2014). https://doi.org/10.1103/PhysRevB.90.224104
46. R. Gaillac, P. Pullumbi, F. X. Coudert, J. Phys.: Cond. Matter **28**, ID 275201 (2016). https://doi.org/10.1088/0953-8984/28/27/275201
47. O. L. Anderson, J. Phys. Chem. Solids **24**, 909 (1963). https://doi.org/10.1016/0022-3697(63)90067-2
48. D. R. Clarke, Surf. Coat. Technol. **164**, 67 (2003). https://doi.org/10.1016/S0257-8972(02)00593-5
49. B. Szpunar, J. I. Ranasinghe, L. Malakkal, and J. A. Szpunar, J. Phys. Chem. Solids **146**, ID 109636 (2020). https://doi.org/10.1016/j.jpcs.2020.109636
50. M. E. Fine, L. D. Brown, H. L. Marcus, Scripta. Met. **18**, 951 (1984). https://doi.org/10.1016/0036-9748(84)90267-9